Published in final edited form as:
Cancer Res. 2010 August 15; 70(16): 6427–6436. doi:10.1158/0008-5472.CAN-10-1350.

Low field magnetic resonance imaging to visualize chronic and cycling hypoxia in tumor-bearing mice

Hironobu Yasui[1], **Shingo Matsumoto**[1], **Nallathamby Devasahayam**[1], **Jeeva P. Munasinghe**[2], **Rajani Choudhuri**[1], **Keita Saito**[1], **Sankaran Subramanian**[1], **James B. Mitchell**[1], and **Murali C. Krishna**[1]

[1]Radiation Biology Branch, Center for Cancer Research, National Cancer Institute

[2]National Institute of Neurological Disorder and Stroke, NIH, Bethesda, MD

Abstract

Tumors exhibit fluctuations in blood flow that influence oxygen concentrations and therapeutic resistance. To assist therapeutic planning and improve prognosis, non-invasive dynamic imaging of spatial and temporal variations in oxygen partial pressure (pO_2) would be useful. Here we illustrate the use of pulsed electron paramagnetic resonance imaging (EPRI) as a novel imaging method to directly monitor fluctuations in oxygen concentrations in mouse models. A common resonator platform for both EPRI and magnetic resonance imaging (MRI) provided pO_2 maps with anatomical guidance and microvessel density. Oxygen images acquired every 3 min for a total of 30 min in two different tumor types revealed that fluctuations patterns in pO_2 are dependent on tumor size and tumor type. The magnitude of fluctuations in pO_2 in SCCVII tumors ranged between 2-18 fold, whereas the fluctuations in HT29 xenografts were of lower magnitude. Alternating breathing cycles with air or carbogen (95 % O_2 plus 5 % CO_2) distinguished higher and lower sensitivity regions which responded to carbogen, corresponding to cycling hypoxia and chronic hypoxia, respectively. Immunohistochemical analysis suggests that the fluctuation in pO_2 correlated with pericyte density rather than vascular density in the tumor. This EPRI technique, combined with MRI, may offer a powerful clinical tool to noninvasively detect variable oxygenation in tumors.

Keywords

Angiogenesis; EPR imaging; Hypoxia; Oxygenation; Tumor

Introduction

Understanding the tumor microenvironment is crucial in the analysis of a solid tumor's response to therapy and in the augmentation of that response. Oxygen status is an important component of the tumor microenvironment. While normal tissues display a well regulated balance between oxygen supply and consumption, in tumors oxygen consumption exceeds delivery, resulting in hypoxia. This situation is attributed mainly to inefficient blood supply caused by morphological and architectural abnormalities in the tumor vasculature that develops during tumor angiogenesis (1). Tumor microvasculature is characterized by loss of hierarchy, heterogeneous vessel distribution, and tortuous vessels with elongated segments (2). Tumor blood vessels typically lack smooth muscle support, as well as an incomplete

Corresponding author: Murali C. Krishna, Radiation Biology Branch, Center for Cancer Research, National Cancer Institute, Building 10, Room B3B69, NIH, 9000 Rockville Pike, Bethesda, Maryland 20892-1002, USA. Phone: (301) 496-7511; Fax: (301) 480-2238, murali@helix.nih.gov.

endothelial lining and basement membrane, making them leaky (3). The abnormal architecture of tumor blood vessels makes them inefficient in delivering oxygen and nutrients, resulting in longitudinal oxygen gradients within the vessels themselves (4).

Based on observations of histological sections of human lung cancer, Thomlinson and Gray hypothesized the presence of hypoxia in tumors as a potential cause of radiation treatment resistance (5). In the 1960s Powers and Tolmach provided direct evidence that hypoxia was present in rodent tumors (6). Subsequently, low oxygen levels, measured with oxygen electrodes inserted into tumors, were correlated with poor radiation treatment outcome in human head and neck cancer (7-9). Recently, many solid tumors have been shown to contain subpopulations of hypoxic cells that limit the efficacy of cancer therapy such as radiation, chemotherapy, and even surgery (8,10). Thus knowledge of tumor oxygen levels has both therapeutic as well as prognostic value that has prompted active research into how to monitor hypoxia *in vivo* and how to sensitize hypoxic regions to radiation (11,12).

In addition to diffusion limited chronic hypoxia, tumors were also shown to experience acute, intermittent, and cycling hypoxia (13,14). Cycling hypoxia was suggested to contribute to tumor progression by providing repeated exposure to hypoxia-reperfusion injury (15-17). Cycling hypoxia in tumors was first documented with indirect methods using dyes permitting a 110 second “snapshot” assessment of blood flow (18). Further studies with double labeling with hypoxia tracers revealed that 8-20% of tumor cells can experience intermittent hypoxia if they are not adjacent to blood vessels (19). Though the flow in tumor vasculature was aberrant, which was attributed to stasis of flow, this phenomenon was not entirely sufficient to explain cycling hypoxia (18).

The first study associating erythrocyte flux with tumor pO_2 was performed using a window chamber model monitoring their flux by fluorescently labeled red blood cells and simultaneously measuring pO_2 by locally placed polarographic electrodes (20). Dewhirst and colleagues established a clear relationship between erythrocyte flux and tumor pO_2 fluctuations at higher frequency within the oxygen diffusion distance (14). Cycling hypoxia was also documented in experimental models using non-invasive approaches such as BOLD contrast MRI, dynamic contrast enhanced MRI and optical probes (21-23). Using positron emission tomography (PET) and ^{18}F-labeled misonidazole as a hypoxia marker, tumor hypoxia was evaluated in patients with head and neck cancer every three days (24). These studies provided evidence that the size and distribution of hypoxic sub-volumes exhibited significant changes over time. Collectively, these studies though qualitative, reinforce the importance of studying acute hypoxia in human tumors to gain a better understanding of fluctuations in tumor physiology.

Electron paramagnetic resonance (EPR) is a spectroscopic technique similar to nuclear magnetic resonance (NMR). EPR detects paramagnetic species that have unpaired electrons. EPR spectroscopy and imaging have been implemented successfully to examine tumor reoxygenation profile after radiation treatment of murine tumors (25,26), to determine tumor cure dependency on hypoxic fraction (27) and examine changes in tumor oxygenation in response to vascular changes (28,29). With the recent availability of triarylmethyl (TAM) radical probes as *in vivo*-compatible tracers (30), EPR imaging (EPRI) is being explored for mapping tissue pO_2 in live animals (31-33). The fundamental basis for EPRI oximetry stems from the paramagnetic nature of O_2 arising from its two unpaired electrons. The collisional interaction between TAM and O_2 broadens the spectral line width of TAM in proportion to oxygen concentration, thereby providing a quantitative measure of tissue pO_2 distribution (34). Since the operating radiofrequency of EPRI is in the same range as that of MRI, it can in principle be applied for human studies.

While EPRI provides maps of pO_2, they lack the anatomic detail available from MRI. A combined EPRI + MRI system overcomes this limitation and provides the necessary anatomic guidance to the pO_2 images. We have recently demonstrated the feasibility of using EPRI coupled with MRI operating at a common frequency of 300 MHz in both modalities with the corresponding magnetic fields at 10 mT (EPRI) and 7 T (MRI). Multiple parameters, including pO_2 map, blood flow, blood volume, water diffusion coefficient, and metabolic profile were obtained from sequential scans to produce a more comprehensive assessment of tumor physiology (35). With subsequent developments in image formation and reconstruction strategies we have made it possible to obtain 3D maps of pO_2 within 3 min in tumors implanted in mice to enable monitoring intermittent hypoxia. In this study, assessment of cycling hypoxia in two different tumor implants in mice was examined by EPRI.

Methods

Animals and tumor implantation

All animal experiments were carried out in compliance with the *Guide for the care and use of laboratory animal resources* (National Research Council, 1996) and approved by the National Cancer Institute Animal Care and Use Committee. Female C3H/Hen mice and athymic nude mice were supplied by the Frederick Cancer Research Center, Animal Production (Frederick, MD). SCCVII and HT29 solid tumors were formed by injecting 5×10^5 cells and 1×10^6 cells subcutaneously into right hind legs of mice. The experiment was initiated on separate sets of animals when their individual tumors grew to ~600, ~1200 and ~1800 mm^3 (the tumor volume = length × $width^2 \times \pi/6$). Mice were anesthetized by isoflurane inhalation (4% for induction and 1.5% for maintaining anesthesia) and positioned prone with their tumor-bearing legs placed inside the resonator. During EPRI and MRI measurements, the breathing rate of the mouse was monitored with a pressure transducer (SA Instruments Inc.) and maintained at 60 ± 10 breaths per minute. Core body temperature was maintained at 37 °C with a flow of warm air.

EPR imaging

Technical details of the EPR scanner and oxygen image reconstruction were described in earlier reports (32,35-38). The description of the resonator (17 mm i.d. and 17 mm long) used as an identical coil for EPRI and MRI operating at 300 MHz was previously described (39,40). After the animal was placed in the resonator, oxygen-sensitive tracer TAM (OX63, GE Healthcare) was injected intravenously. Pharmacological decrease of the tracer was prevented by continuous injection of TAM into mice (41). TAM was given as a 1.125 mmol/kg bolus followed by 0.04 mmol/kg/min continuous injection.

The FID signals were collected following the radiofrequency (RF) excitation pulses (80 ns, 80 W, 70° flip angle) under a nested looping of the x, y, z gradients and each time point in the FID underwent phase modulation enabling 3D spatial encoding. The repetition time (TR) was 6.0 μs. Since FIDs last for a couple of microseconds, it is possible to generate a sequence of T_2* maps i.e. EPR line width maps, which allowed pixel-wise estimation of pO_2. The spatial resolution was 1.6~1.8 mm, although the pixel resolution was digitally enhanced to co-register with MRI images. Minimum signal to noise ratio used for reliable pO_2 estimation is about 30.

Co-registration of pO_2 images from EPRI with anatomic images from 7T MRI

MRI scans were conducted using a 7 T scanner controlled with ParaVision 5.0 (Bruker BioSpin MRI GmbH). After a quick assessment of the sample position by a fast low-angle shot (FLASH) tripilot sequence, T_2-weighted anatomical images were obtained using a fast

spin echo sequence (RARE) with an echo time (TE) of 13 ms, TR of 2500 ms, 16 slices, RARE factor 8, resolution of 0.125 × 0.25 mm. For convenience of coregistration with EPRI, all MRI images had the same FOV of 3.2 cm and slice thickness of 2 mm. For blood volume calculation, spoiled gradient echo (SPGR) sequence images were collected before and 5 min after ultra small superparamagnetic iron oxide (USPIO, Molday ION, BioPAL Inc.) injection (1.2 μL /g body weight) with following parameters: matrix = 256 × 256; TE = 5.4 ms; TR = 250 ms. Percentage of tumor blood volume was estimated by the expression $100 \times (S_{pre} - S_{post}) / [S_{pre} + S_{post} (W_b/W_t - 1)]$, where S_{pre} and S_{post} were the signal intensities before and after USPIO injection and W_b and W_t were the intra- and extravascular water fractions (35,42). Co-registration of EPRI and MRI images was accomplished using code written in MATLAB (Mathworks) as described previously (35,37).

Immunohistochemical analysis

A hypoxia marker, pimonidazole (43) was given intravenously between EPRI and MRI scans. After MRI study, the perfusion marker Hoechst33342 was injected. Two minutes later, mice were euthanized and tumor tissues were excised at the same tilt angle and depth from the surface in coincidence with the MRI images as reported previously with slight modification (44). Tumor tissues were fixed with 4% paraformaldehyde, frozen, and 10 μm thick sections were obtained. Tissue sections were air-dried, and then the Hoechst33342 signal was recorded. After blocking non-specific binding sites, the slides were covered by CD31 antibody (BD Biosciences, San Jose, CA; 1:250) combined with αSMA antibody (Abcam Inc., Cambridge, MA; 1:250) or rabbit anti-pimonidazole antisera (Natural Pharmacia International, Inc., Burlington, MA; 1:250) overnight at 4°C. The sections were incubated with Alexa Fluor 488 anti-rat and Alexa Fluor 555 anti-rabbit secondary antibody (Invitrogen, Carlsbad, CA; 1:500). Then they were mounted on Prolong Gold antifade reagent with DAPI (Invitrogen). Fluorescence microscopic observation was performed using an Axiovert 200 inverted fluorescent microscope (Carl Zeiss). Serial sections were also stained with hematoxylin and eosin.

The quantification of CD31 and αSMA was performed according to the method described by Zhou et al. (45). Briefly, tissue sections were viewed at ×200 magnification and more than three fields per section were captured using Image-Pro Plus Ver. 4.0 imaging software. Then the quantification of vascular density and pericyte density on each image was performed using the ImageJ software package (46) and shown as the total number of positive pixels per field.

Statistical analysis

All results were expressed as the mean ± S.E. The differences in means of groups were determined by Mann–Whitney U test using Stat View 5.0 J software (SAS Institute Inc., Cary, NC). The minimum level of significance was set at $P<0.05$.

Results

Non-invasive imaging of oxygen fluctuation in SCCVII and HT29 tumors by rapid EPRI scan

To examine the spatial distribution of tumor pO_2 and monitor temporal pO_2 fluctuations, sequential EPRI and MRI experiments on tumor-bearing mice were conducted using a resonator assembly tuned to the common frequency of 300 MHz for both modalities. Figure 1A shows eight adjacent slices of anatomic images from MRI and Figure 1B shows the corresponding pO_2 images from EPRI after infusion of oxygen sensing paramagnetic tracer TAM in the SCCVII tumor. Each MRI slice was 2 mm thick and the corresponding pO_2 image slice was selected from the 3D image data of EPRI. Marked heterogeneity in pO_2

levels was observed throughout the tumor, with pO_2 levels ranging from 0 – 35 mmHg. The tumor exhibited a significant hypoxic core, surrounded by normoxic regions.

To examine the spatial and temporal changes in tumor physiology, two separate models were chosen; a SCCVII murine carcinoma and a HT29 human colon carcinoma. To visualize dynamic changes of tumor oxygenation over a time period of 30 min, EPRI experiments were carried out collecting nine image data sets, each taking ~3 min, for a 3D reconstruction of pO_2 maps as well as the tracer distribution. Figure 2A shows the anatomic image of a SCCVII tumor obtained from MRI with four regions of interest (ROI) indicated. Figure 2B shows the corresponding time-dependent changes in pO_2 (top row) and the levels of TAM (bottom row) obtained by EPRI (animation is available in the supplemental movie 1). It should be noted that pO_2 values can be determined quantitatively independent of differing levels of the tracer TAM in different regions, provided the tracer EPR signals are detectable (32, 35, 36). The tumor oxygen levels displayed significant fluctuations, while the tracer level during this time window remained relatively stable. When tumor oxygen levels and TAM tracer levels in the four ROIs identified in the anatomic image (Figure 2A) were plotted as a function of time, ROIs 1 and 2 displayed significant fluctuations in pO_2 (~ 18 fold and 12 fold respectively), while ROIs 3 and 4 displayed relatively smaller changes (~ 2 fold). No significant changes in the TAM tracer level were observed across the time course (Figure 2C, right). Comparing the pO_2 maps and the tracer levels as a function of time (Figure 2B and C), it can be seen in ROI 4 that the tracer level was adequate enough for detection and imaging, yet this region displayed significant hypoxia. On the other hand, in the three remaining ROIs where the tracer level was high and stable, the pO_2 fluctuations with time were significant, supporting previous observations of cycling hypoxia resulting from fluctuations in red blood cell flux (14).

Similar studies were conducted on the human tumor HT29 cell line. Anatomic images were obtained by T_2-weighted MRI, and four ROIs were identified (Figure 3A). The spatial distribution of pO_2 is shown in Figure 3B, and the pO_2 values against time are plotted in Figure 3C. All four ROIs displayed time-dependent fluctuations, though of a smaller magnitude than that observed with the SCCVII tumors. Once again, TAM was distributed throughout the tumor and remained relatively stable, while the fluctuations of oxygen occurred (Figure 3B and C, Supplemental movie 1). ROI 4, which had a higher level of the TAM tracer than ROI 1 and 3, exhibited pO_2 levels < 10 mm Hg. This phenomenon was similar to that observed in SCCVII tumor, where in spite of adequate level of tracer, significant hypoxia existed in certain regions of the tumor. The TAM tracer level was reported to be spatially correlated with increased tumor microvascular permeability, i.e. abnormality of tumor blood vessels, whose distribution was in turn matched with hypoxic regions (44). This behavior may be a result of longitudinal oxygen gradient, whereas plasma flow may be not significantly impeded resulting in adequate tracer levels but with significant hypoxia. Collectively, the results shown in Figures 2 and 3 support the use of EPRI for monitoring dynamic changes in oxygen levels in tumors.

Decrease in oxygenation and blood volume is dependent on tumor size

In general, tumor size/stage largely determines the tumor physiology and may contribute to the outcome of cancer therapy. Previous studies reported that the degree of hypoxia and inadequacy of vascularity increased with increasing tumor size (47,48). To examine this phenomenon non-invasively, mice were divided into three groups by their tumor sizes (<600 mm^3, 600~1200 mm^3 and >1200 mm^3) and evaluated using EPRI for pO_2 and MRI for anatomy and blood volume. Figure 4A shows the tumor pO_2 maps and images of blood volume, from a representative SCCVII tumor. From the EPRI maps, the averaged tumor pO_2 was found to decrease gradually with increasing tumor size. The pO_2 levels were 14.8 ± 1.1 mmHg for the smallest tumor, 12.7 ± 1.1 mmHg for the medium-size tumor, and 12.4 ± 0.7

mmHg for the largest tumor. Consistently, the fractional hypoxic volume (% volume with pO_2 < 10 mmHg) increased with tumor size and reached 41.0 ± 2.6% in the largest tumor compared with 20.9 ± 6.2% in the smallest tumor. Comparing identical regions of the corresponding MR images, we examined the blood volume as a non-invasive indicator of microvessel density using the blood pool T_2 contrast agent USPIO (42). For small tumors, the blood vessel coverage was relatively uniform, with a density of 27.7 ± 2.1%. However, blood vessels in the largest tumor displayed significant heterogeneity and their density decreased to 8.1 ± 2.0%. Similar patterns of decreasing blood vessel density and pO_2 were observed with increasing tumor size in HT29 tumors, though in this case the changes were not statistically significant (Figure 4B).

Oxygen fluctuations are dependent on tumor size and tumor type

We next examined the relationship of fluctuation of tumor pO_2 with tumor size and tumor type. The intrapixel standard deviations of pO_2 (pO_2 SD) from the nine pO_2 images collected between 4 and 28 min were computed. The pO_2 SD values over the time period studied for SCCVII tumors were found to increase from 4.6 ± 0.3 mmHg in the <600 mm^3 group to 6.4 ± 0.7 mmHg in the >1200 mm^3 group (correlation coefficient r = 0.61, p = 0.059) (Figure 5A). Interestingly, pO_2 SD in HT29 tumor underwent comparatively smaller changes as a function of tumor size (3.7 ± 0.2 mmHg for <600 mm^3 group and 4.1 ± 0.5 mmHg in >1200 mm^3 group, respectively). When pO_2 fluctuations were compared in two different tumor types at the same size, the pO_2 SD of the SCCVII tumor was found to be larger than that of the HT29 tumor at all sizes (<600 mm^3; p = 0.0318, >1200 mm^3; p = 0.0298) (Figure 5A). These results suggested that the tumor size dependent variations in pO_2 are dependent on the tumor type.

Oxygen fluctuation was not influenced by vascular density but by maturation

To investigate whether vascular density and/or maturity of the tumor vasculature contributes to tumor type-dependent differences in oxygen fluctuations, immuno-histochemical analyses for CD31 and αSMA as markers of endothelial cells and pericytes respectively, were performed (Figure 5B). Though the tumor type dependent difference in the vascular density (CD31, green) was negligible (3.6 ± 0.2% for SCCVII and 3.5 ± 0.2% for HT29), a difference in the pericyte coverage density (αSMA, red) between SCCVII and HT29 tumors was apparent. In the SCCVII tumor, the number of recruited pericytes was smaller (0.8 ± 0.1% for SCCVII and 13.1 ± 2.9% for HT29) and the coverage of blood vessels with pericytes was relatively less compared to the HT29 tumors (Figure 5C). An earlier study found no correlation between vessel maturation and fluctuations in pO_2 as assessed by T_2*-weighted MRI; these differences with the present study may result from a different tumor model or the measurement type employed (22).

Effect of carbogen breathing on tumor oxygenation

SCCVII tumor-bearing mice were subjected to an air-carbogen (95% O_2 plus 5% CO_2)-air breathing cycle to determine whether tumor pO_2 would change as a function of time. EPRI-derived pO_2 maps were collected during each cycle as shown in Figure 6A. Figure 6B shows the corresponding anatomic image from MRI image from which 3 ROIs were chosen and the pO_2 difference image which is the pO_2 image while breathing air subtracted from pO_2 image while breathing carbogen. The pO_2 values in these three regions were plotted as a function of time (Figure 6C). While comparatively small fluctuations occurred during the air breathing phase (0-12 min), when subjected to carbogen breathing (12-24 min), ROIs 2 and 3 displayed a marked increase in pO_2; whereas, ROI 1 displayed negligible changes (Figure 6C). ROIs 2 and 3 again responded when the breathing gas was restored to air by displaying a steady decrease, whereas ROI 1 was unresponsive. The median pO_2 value was 7.2 mmHg during initial air breathing, and increased to 13.1 mmHg at 19 min by carbogen breathing.

Re-breathing of air moderately decreased the median pO_2 to 8.0 mmHg at 31 min. Frequency histograms of the global tumor pO_2 at selected time points of the air-carbogen-air cycle are shown in Figure 6D. There is a region at low pO_2 values in the histogram which is unresponsive to changes of breathing gas, whereas a right shift of the frequency histogram resulted when carbogen was the breathing gas. Together, these data provide non-invasive experimental evidence to support the notion that diffusion limited chronic hypoxic regions, as well as regions that vary from the extremely hypoxic to the normoxic state, exist in tumors; i.e. cycling hypoxia. The supplementary movie 2 shows representative images of pO_2 maps as a function of time during the air-carbogen-air cycle.

Discussion

Strong experimental evidence obtained using *ex vivo* analyses and window chamber models support the existence of cycling hypoxia in addition to chronic hypoxia in tumor implants in mice and even in human tumors (13,14). The more malignant phenotype associated with cycling hypoxia (15,17) makes a strong case to develop non-invasive imaging techniques to identify such behaviors *in vivo*. EPRI is a non-invasive low field magnetic resonance imaging technique, which uses paramagnetic tracers. Distribution of the tracer and quantitative pO_2 maps can be obtained by monitoring the collisional interactions between the tracer and O_2 molecule (32,35). Sequential imaging with MRI using a common resonator permits reliable co-registration of the pO_2 map with different physiological and metabolic images, and provides a more comprehensive assessment of the tumor microenvironment (35).

Compared with other clinically used methods of assessing tumor oxygen status, EPRI has intrinsic advantages. Unlike polarographic measurements which are invasive and used only in accessible sites but provide quantitative pO_2 assessments from limited sampling volume, EPRI provides similar quantitative information of three-dimensional maps non-invasively. Another oxygen imaging technique, PET, where the hypoxic tracer needs to be internalized and metabolized to bind to hypoxic regions, is not capable of absolute oxygen quantification. Additionally, unlike with EPRI where temporal pO_2 fluctuations in order of minutes can be recognized, PET based methods can only integrate the periods of hypoxia during the scan period.

In the present study, significant fluctuations in tumor pO_2 were seen even with a 3 minute “snapshot”. In the SCCVII transplant, while the fluctuations in the tracer level were minimal throughout the tumor, the pO_2 fluctuations showed significant fluctuations (~30 mmHg) in some regions while other regions displayed fluctuations to a lesser extent. Some regions that were hypoxic (pO_2 <10 mmHg) remained invariant in the time window of observation, suggesting that these regions may result from diffusion-limited chronic hypoxia. In the HT29 xenograft, the extent of fluctuations in pO_2 was found to be smaller than SCCVII transplants. From EPRI studies as a function of tumor growth, it was found that both SCCVII and HT29 tumors showed increasing size of the hypoxic core with a concomitant decrease in the microvessel density. Since several images were collected during the imaging time window and the pO_2 levels determined at each time point, it was possible to obtain images of the standard deviation of the pO_2 calculated over time which would reflect the fluctuations. There was an increase in “pO_2 SD” values with increases in size, in agreement with the studies of Chaplin et al. where cycling hypoxia was not observed in small murine tumors, whereas larger sized tumors (>500 mg) displayed cycling hypoxic behavior (13). These fluctuations appear to be related to the decrease in coverage with pericytes as shown in Figure 5.

Histological analyses after imaging experiments were conducted to assess microvessel density, pericyte coverage, hypoxia, and cell viability to characterize the tumor non-invasively as well as at a microscopic level (Supplemental Figure 1). The agreement between EPRI and histological studies for hypoxia, microvessel density and cell viability support the reliability of the pO_2 assessment capability of EPRI to monitor spatial and temporal fluctuations in pO_2 in tumor transplants. The possibility that EPRI can utilize the significant experience from MRI to scale up for human use makes it a promising modality for integration into radiation treatment planning such as dose-painting based on oxygen maps to selectively deliver higher doses to hypoxic regions (49, 50). Since EPRI can distinguish between cycling hypoxia and chronic hypoxia, individualized treatments to tailor the dose to deliver therapeutic doses uniformly to the tumor appear to be achievable.

Our studies described in this report suggest that the methodology developed here has the capability to monitor pO_2 in tumor implants non-invasively and longitudinally, and examine the onset of cycling hypoxia as a function of tumor growth. Such studies along with the wealth of information available from earlier studies can provide improved understanding of the role of cycling hypoxia in treatment resistance and metastatic potential.

Supplementary Material

Refer to Web version on PubMed Central for supplementary material.

Acknowledgments

This research was supported by the Intramural Research Program, Center for Cancer Research, National Cancer Institute, NIH. We acknowledge the help of Dr Melissa Stauffer (Scientific Editing Solutions) for her editorial help.

References

1. Folkman J. Angiogenesis: an organizing principle for drug discovery? Nat Rev Drug Discov. 2007; 6:273–86. [PubMed: 17396134]
2. Fukumura D, Jain RK. Tumor microvasculature and microenvironment: targets for anti-angiogenesis and normalization. Microvasc Res. 2007; 74:72–84. [PubMed: 17560615]
3. Jain RK. Transport of molecules across tumor vasculature. Cancer Metastasis Rev. 1987; 6:559–93. [PubMed: 3327633]
4. Dewhirst MW, Ong ET, Braun RD, et al. Quantification of longitudinal tissue pO2 gradients in window chamber tumours: impact on tumour hypoxia. Br J Cancer. 1999; 79:1717–22. [PubMed: 10206282]
5. Thomlinson RH, Gray LH. The histological structure of some human lung cancers and the possible implications for radiotherapy. Br J Cancer. 1955; 9:539–49. [PubMed: 13304213]
6. Powers WE, Tolmach LJ. A multicomponent x-ray survival curve for mouse lymphosarcoma cells irradiated in vivo. Nature. 1963; 197:710–1. [PubMed: 13985844]
7. Gatenby RA, Kessler HB, Rosenblum JS, et al. Oxygen distribution in squamous cell carcinoma metastases and its relationship to outcome of radiation therapy. Int J Radiat Oncol Biol Phys. 1988; 14:831–8. [PubMed: 3360652]
8. Hockel M, Schlenger K, Aral B, et al. Association between tumor hypoxia and malignant progression in advanced cancer of the uterine cervix. Cancer Res. 1996; 56:4509–15. [PubMed: 8813149]
9. Brizel DM, Dodge RK, Clough RW, Dewhirst MW. Oxygenation of head and neck cancer: changes during radiotherapy and impact on treatment outcome. Radiother Oncol. 1999; 53:113–7. [PubMed: 10665787]
10. Dewhirst MW. Relationships between cycling hypoxia, HIF-1, angiogenesis and oxidative stress. Radiat Res. 2009; 172:653–65. [PubMed: 19929412]

11. Brown JM. The hypoxic cell: a target for selective cancer therapy--eighteenth Bruce F. Cain Memorial Award lecture. Cancer Res. 1999; 59:5863–70. [PubMed: 10606224]
12. Brown JM. Hypoxic cytotoxic agents: a new approach to cancer chemotherapy. Drug Resist Updat. 2000; 3:7–13. [PubMed: 11498360]
13. Chaplin DJ, Olive PL, Durand RE. Intermittent blood flow in a murine tumor: radiobiological effects. Cancer Res. 1987; 47:597–601. [PubMed: 3791244]
14. Kimura H, Braun RD, Ong ET, et al. Fluctuations in red cell flux in tumor microvessels can lead to transient hypoxia and reoxygenation in tumor parenchyma. Cancer Res. 1996; 56:5522–8. [PubMed: 8968110]
15. Cairns RA, Kalliomaki T, Hill RP. Acute (cyclic) hypoxia enhances spontaneous metastasis of KHT murine tumors. Cancer Res. 2001; 61:8903–8. [PubMed: 11751415]
16. Cairns RA, Hill RP. Acute hypoxia enhances spontaneous lymph node metastasis in an orthotopic murine model of human cervical carcinoma. Cancer Res. 2004; 64:2054–61. [PubMed: 15026343]
17. Cairns RA, Khokha R, Hill RP. Molecular mechanisms of tumor invasion and metastasis: an integrated view. Curr Mol Med. 2003; 3:659–71. [PubMed: 14601640]
18. Chaplin DJ, Trotter MJ, Durand RE, Olive PL, Minchinton AI. Evidence for intermittent radiobiological hypoxia in experimental tumour systems. Biomed Biochim Acta. 1989; 48:S255–9. [PubMed: 2730619]
19. Bennewith KL, Durand RE. Quantifying transient hypoxia in human tumor xenografts by flow cytometry. Cancer Res. 2004; 64:6183–9. [PubMed: 15342403]
20. Braun RD, Lanzen JL, Dewhirst MW. Fourier analysis of fluctuations of oxygen tension and blood flow in R3230Ac tumors and muscle in rats. Am J Physiol. 1999; 277:H551–68. [PubMed: 10444480]
21. Baudelet C, Ansiaux R, Jordan BF, et al. Physiological noise in murine solid tumours using T2*-weighted gradient-echo imaging: a marker of tumour acute hypoxia? Phys Med Biol. 2004; 49:3389–411. [PubMed: 15379021]
22. Baudelet C, Cron GO, Ansiaux R, et al. The role of vessel maturation and vessel functionality in spontaneous fluctuations of T2*-weighted GRE signal within tumors. NMR Biomed. 2006; 19:69–76. [PubMed: 16411170]
23. Brurberg KG, Thuen M, Ruud EB, Rofstad EK. Fluctuations in pO2 in irradiated human melanoma xenografts. Radiat Res. 2006; 165:16–25. [PubMed: 16392958]
24. Wang K, Yorke E, Nehmeh SA, Humm JL, Ling CC. Modeling acute and chronic hypoxia using serial images of 18F-FMISO PET. Med Phys. 2009; 36:4400–8. [PubMed: 19928070]
25. Goda F, Bacic G, O'Hara JA, et al. The relationship between partial pressure of oxygen and perfusion in two murine tumors after X-ray irradiation: a combined gadopentetate dimeglumine dynamic magnetic resonance imaging and in vivo electron paramagnetic resonance oximetry study. Cancer Res. 1996; 56:3344–9. [PubMed: 8764132]
26. Goda F, O'Hara JA, Rhodes ES, et al. Changes of oxygen tension in experimental tumors after a single dose of X-ray irradiation. Cancer Res. 1995; 55:2249–52. [PubMed: 7757972]
27. Elas M, Bell R, Hleihel D, et al. Electron paramagnetic resonance oxygen image hypoxic fraction plus radiation dose strongly correlates with tumor cure in FSa fibrosarcomas. Int J Radiat Oncol Biol Phys. 2008; 71:542–9. [PubMed: 18474313]
28. Ansiaux R, Baudelet C, Jordan BF, et al. Thalidomide radiosensitizes tumors through early changes in the tumor microenvironment. Clin Cancer Res. 2005; 11:743–50. [PubMed: 15701864]
29. Jordan BF, Gregoire V, Demeure RJ, et al. Insulin increases the sensitivity of tumors to irradiation: involvement of an increase in tumor oxygenation mediated by a nitric oxide-dependent decrease of the tumor cells oxygen consumption. Cancer Res. 2002; 62:3555–61. [PubMed: 12068004]
30. Ardenkjaer-Larsen JH, Laursen I, Leunbach I, et al. EPR and DNP properties of certain novel single electron contrast agents intended for oximetric imaging. J Magn Reson. 1998; 133:1–12. [PubMed: 9654463]
31. Elas M, Williams BB, Parasca A, et al. Quantitative tumor oxymetric images from 4D electron paramagnetic resonance imaging (EPRI): methodology and comparison with blood oxygen level-dependent (BOLD) MRI. Magn Reson Med. 2003; 49:682–91. [PubMed: 12652539]

32. Matsumoto K, Subramanian S, Devasahayam N, et al. Electron paramagnetic resonance imaging of tumor hypoxia: enhanced spatial and temporal resolution for in vivo pO2 determination. Magn Reson Med. 2006; 55:1157–63. [PubMed: 16596636]
33. Elas M, Ahn KH, Parasca A, et al. Electron paramagnetic resonance oxygen images correlate spatially and quantitatively with Oxylite oxygen measurements. Clin Cancer Res. 2006; 12:4209–17. [PubMed: 16857793]
34. Lai CS, Hopwood LE, Hyde JS, Lukiewicz S. ESR studies of O2 uptake by Chinese hamster ovary cells during the cell cycle. Proc Natl Acad Sci U S A. 1982; 79:1166–70. [PubMed: 6280170]
35. Matsumoto S, Hyodo F, Subramanian S, et al. Low-field paramagnetic resonance imaging of tumor oxygenation and glycolytic activity in mice. J Clin Invest. 2008; 118:1965–73. [PubMed: 18431513]
36. Devasahayam N, Subramanian S, Murugesan R, et al. Strategies for improved temporal and spectral resolution in in vivo oximetric imaging using time-domain EPR. Magn Reson Med. 2007; 57:776–83. [PubMed: 17390350]
37. Dharmaraj CD, Thadikonda K, Fletcher AR, et al. Reconstruction for Time-Domain In Vivo EPR 3D Multigradient Oximetric Imaging-A Parallel Processing Perspective. Int J Biomed Imaging. 2009; 2009:528639. [PubMed: 19672315]
38. Subramanian S, Devasahayam N, Murugesan R, et al. Single-point (constant-time) imaging in radiofrequency Fourier transform electron paramagnetic resonance. Magn Reson Med. 2002; 48:370–9. [PubMed: 12210946]
39. Devasahayam N, Subramanian S, Murugesan R, et al. Parallel coil resonators for time-domain radiofrequency electron paramagnetic resonance imaging of biological objects. J Magn Reson. 2000; 142:168–76. [PubMed: 10617448]
40. Hyodo F, Matsumoto S, Devasahayam N, et al. Pulsed EPR imaging of nitroxides in mice. J Magn Reson. 2009; 197:181–5. [PubMed: 19157932]
41. Matsumoto K, English S, Yoo J, et al. Pharmacokinetics of a triarylmethyl-type paramagnetic spin probe used in EPR oximetry. Magn Reson Med. 2004; 52:885–92. [PubMed: 15389949]
42. Hyodo F, Chandramouli GV, Matsumoto S, et al. Estimation of tumor microvessel density by MRI using a blood pool contrast agent. Int J Oncol. 2009; 35:797–804. [PubMed: 19724915]
43. Azuma C, Raleigh JA, Thrall DE. Longevity of pimonidazole adducts in spontaneous canine tumors as an estimate of hypoxic cell lifetime. Radiat Res. 1997; 148:35–42. [PubMed: 9216616]
44. Matsumoto S, Yasui H, Batra S, et al. Simultaneous imaging of tumor oxygenation and microvascular permeability using Overhauser enhanced MRI. Proc Natl Acad Sci U S A. 2009; 106:17898–903. [PubMed: 19815528]
45. Zhou Q, Guo P, Gallo JM. Impact of angiogenesis inhibition by sunitinib on tumor distribution of temozolomide. Clin Cancer Res. 2008; 14:1540–9. [PubMed: 18316579]
46. ImageJ: Image processing and analysis in Java. http://rsb.info.nih.gov/ij/
47. Hendriksen EM, Span PN, Schuuring J, et al. Angiogenesis, hypoxia and VEGF expression during tumour growth in a human xenograft tumour model. Microvasc Res. 2009; 77:96–103. [PubMed: 19118564]
48. Sorg BS, Moeller BJ, Donovan O, Cao Y, Dewhirst MW. Hyperspectral imaging of hemoglobin saturation in tumor microvasculature and tumor hypoxia development. J Biomed Opt. 2005; 10:44004. [PubMed: 16178638]
49. Lin Z, Mechalakos J, Nehmeh S, et al. The influence of changes in tumor hypoxia on dose-painting treatment plans based on 18F-FMISO positron emission tomography. Int J Radiat Oncol Biol Phys. 2008; 70:1219–28. [PubMed: 18313529]
50. Leibel SA, Fuks Z, Zelefsky MJ, et al. Intensity-modulated radiotherapy. Cancer J. 2002; 8:164–76. [PubMed: 12004802]

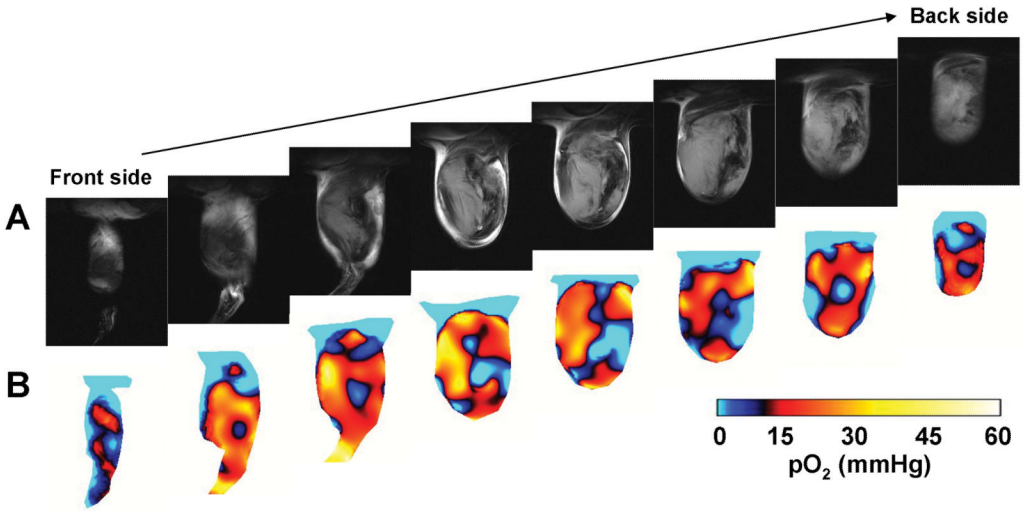

Figures 1.

3D oxygen image in a SCCVII tumor using EPRI. (A) Anatomical images of SCCVII tumor bearing leg obtained by T_2-weighted 7T MRI. (B) Oximetric images acquired by pulsed EPRI. Both MRI and EPRI scans were performed using an identical coil operating at 300 MHz. The images were serially displayed at every 2 mm from front side to back side in both modalities.

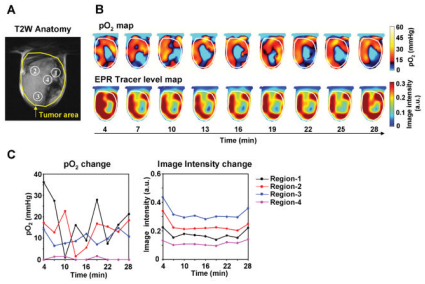

Figure 2.

Non-invasive imaging of fluctuating pO_2 in SCCVII tumors using EPRI. (A) T_2-weighted anatomical image of a representative SCCVII tumor-bearing mouse. Large yellow line indicates tumor region. Four ROIs indicated by small white line were chosen for tracing fluctuations of pO_2 and spin intensity with time. (B) Corresponding pO_2 maps (upper panels) and the tracer level maps (lower panels) were obtained from EPRI. Tumor region was shown by while line. Time increased from left to right from 4 min to 28 min. (C) The values of pO_2 and the tracer level in each ROI region, described in Fig. 2A, were quantified and plotted as a function of time.

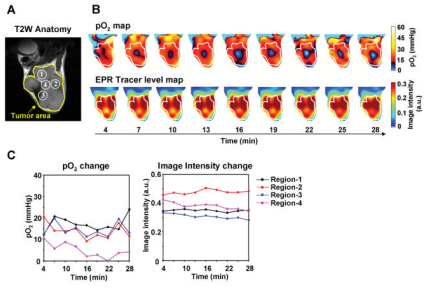

Figure 3.

Non-invasive imaging of fluctuating pO_2 in HT29 tumors. (A) T_2-weighted anatomical image of a representative HT29 tumor-bearing mouse. (B) Corresponding pO_2 maps (upper panels) and the tracer level maps (lower panels) were obtained from EPRI. (C) The values of pO_2 and the tracer level in each ROI region, described in Fig. 3A, were plotted as a function of time.

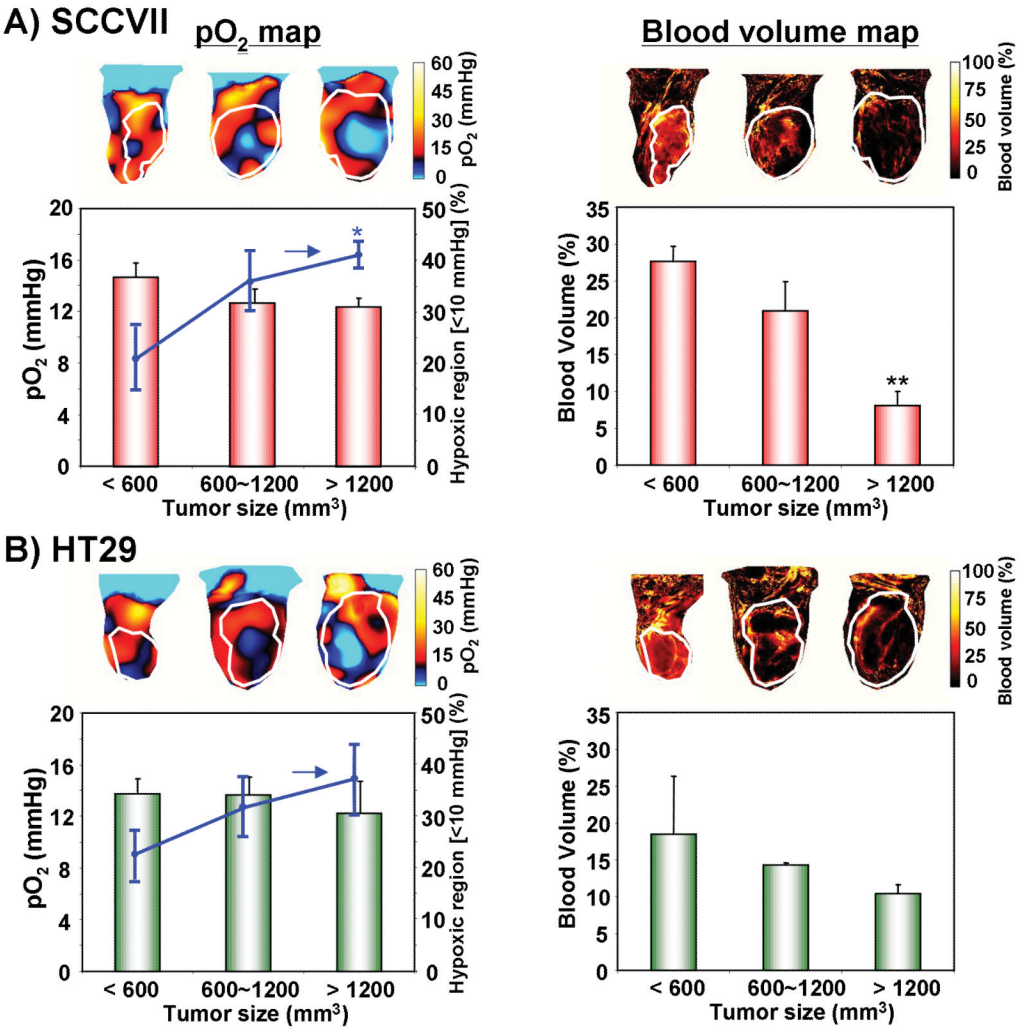

Figure 4.

The effects of tumor type and size on oxygenation and blood volume. Median tumor pO_2 and the percentage of hypoxic region were estimated from EPRI in **(A)** SCCVII and **(B)** HT29 tumors. Representative pO_2 maps at three tumor sizes are shown in the left upper panels. Tumor pO_2 values from at least three tumors at each size are shown in red bar graphs (n = 3-4). The hypoxic volume, the percentage of the tumor volume having pO_2 less than 10 mmHg, was plotted as a line superimposed on the bar graphs (n = 3-4). Blood volume images (right panels) were obtained from MRI studies using USPIO (n = 3-4).

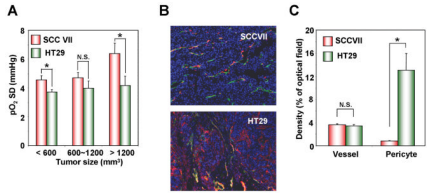

Figure 5.

(A) The standard deviation of pO_2 over time (pO_2 SD) at each pixel was calculated from nine pO_2 images obtained from 4 min to 28 min after TAM injection in SCCVII (red) and HT29 (green) tumors (n = 3-4). **(B)** Representative images of double immunofluorescence staining for CD31 (green) and αSMA (red) as makers of endothelial cells and pericytes, respectively. The vessels covered with αSMA were indicated as merged yellow cells. **(C)** CD31 and αSMA densities were quantified as the percentage of fluorescence-positive area (n = 3-4).

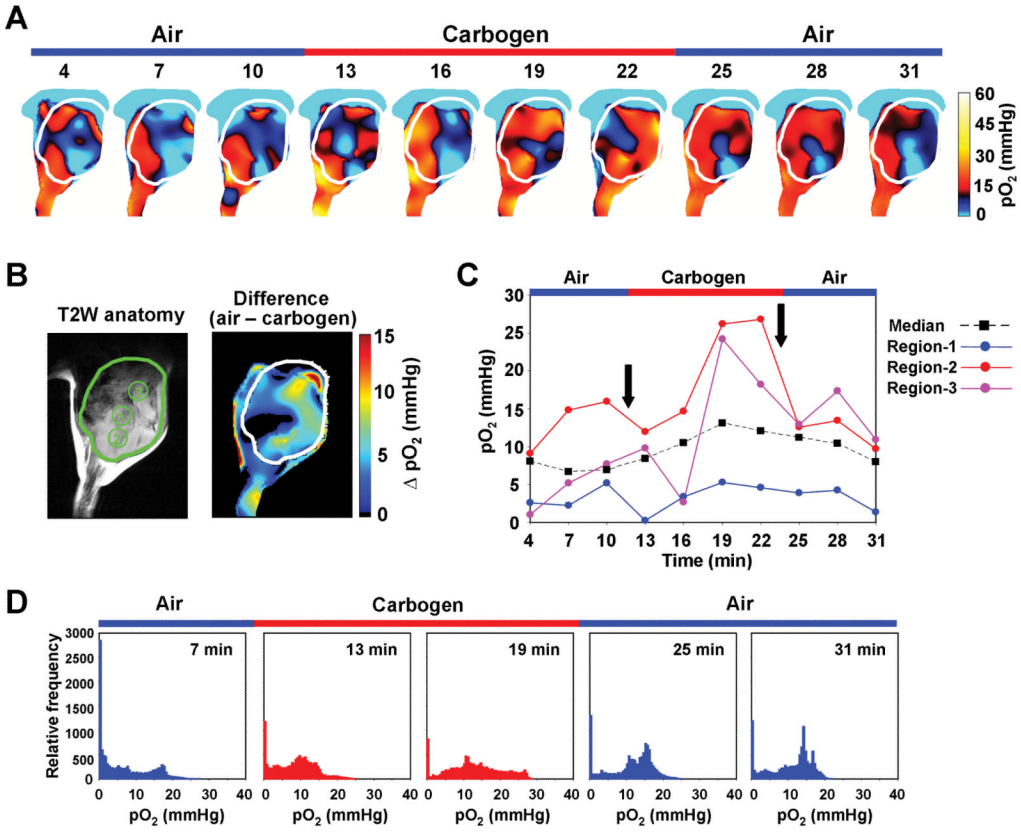

Figure 6.

The dynamic monitoring of the effect of carbogen breathing on tumor oxygenation. **(A)** Representative time-serial pO_2 maps in a SCCVII tumor. Time increased from left to right from 4 min to 31 min. The breathing gas changed from air to carbogen at 12 min after the TAM injection, and changed back to air at 24 min. **(B)** Anatomical image using T_2-weighted MRI (left panel) and pO_2 difference map (right panel) obtained by subtracting averaged pO_2 maps while breathing air from averaged pO_2 maps while breathing carbogen. The tumor region is indicated by the contour. Three ROIs indicated by numbers were chosen for monitoring temporal pO_2 change. **(C)** The pO_2 values in each ROI and the median pO_2 of the whole tumor region at each time point. **(D)** Temporal series of pO_2 histograms in tumor region at every 6 min. Red histograms at 13 and 19 min indicate tumor oxygen status under carbogen breathing.